

An equivalent source method for removal of attitude-induced responses in drone-towed magnetic scalar gradiometry data

Jacob Thejll Petersen,¹ Mick E. Kolster¹,^{ORCID} Thorkild M. Rasmussen² and Arne Døssing¹

¹CMAGTRES, Geomagnetisme and Geospace, DTU Space, Technical University Denmark, Centrifugevej 356, 2850 Kgs. Lyngby, Denmark.

E-mail: jacth@space.dtu.dk

²Department of Civil, Environmental and Natural Resources Engineering Luleå Technical University, 97187 Luleå, Sweden

Accepted 2022 October 11. Received 2022 September 16; in original form 2022 March 23

SUMMARY

Drone-towed scalar field gradiometry surveys conducted in windy conditions or under self-excited oscillations generate attitude-induced responses that can hinder the geological interpretation. Here, we present a gradiometric equivalent source method (GESM) to remove these attitude-induced responses by interpolating and continuing the measured gradiometry data to new idealized pseudo-sensor positions free of any attitude deviations. In addition, we present transverse horizontal difference (THD) data from a precisely positioned drone-towed horizontal gradiometry survey collected in Nautanen, northern Sweden. Analysing the Nautanen survey's positional data revealed that the gradiometer system exhibited directional-dependent yaw deviations with periods of unpredictable attitude deviations. Based on synthetic THD data created using the Nautanen survey's positional data, these deviations manifest as line-to-line striping and short-wavelength oscillations in the THD maps. Applying GESM to the synthetic THD data removes these attitude-induced THD responses with satisfactory accuracy compared to the true THD values. Furthermore, on the actual THD data collected in Nautanen, applying GESM improved the continuity of anomalies, significantly improving the interpretation of the data. The results suggest that applying GESM to drone-towed gradiometry surveys, given precise attitude information via an onboard GNSS-IMU system, maintains high quality even when surveying in windy conditions or in high-gradient areas. The results suggest that including GESM in the data processing of drone-towed gradiometry surveys, given precise positional information via an onboard GNSS-IMU system, ensures high-quality geological interpretation even in windy conditions or in high-gradient areas.

Key words: Electromagnetic theory; Magnetic anomalies; modelling and interpretation; Inverse theory; Crustal structure; Drone-towed magnetic surveying; Equivalent source method.

1 INTRODUCTION

Aeromagnetic surveying is an established geophysical approach for mineral exploration, commonly carried out using magnetometers aboard a small fixed-wing aircraft or towed underneath a helicopter in a so-called magnetometer bird. Fixed-wing aircraft are primarily used for regional-scale surveying purposes, while heliborne magnetometer bird systems are preferred for high-resolution, topography-draped surveying.

Aeromagnetic short-baseline gradiometry surveys, where two or more magnetometers are deployed simultaneously, have been carried out since the 1970s. This advanced survey approach was facilitated by the development of optically pumped survey magnetometers, which were more sensitive as compared to proton precession magnetometers (Hood 1965; Hood *et al.* 1979; Cowan *et al.*

1995). A gradiometer system measures the scalar field differences between two magnetometers across a short baseline thereby quantifying the scalar field variation. Measurements of the scalar field difference have significant advantages over scalar-field measurements, including the elimination of the external field variations and enhancement of shallow anomalies by filtering out regional sources (Cowan *et al.* 1995). The first gradiometer systems were deployed by the Geological Survey of Canada and typically comprised an inboard vertical gradiometer system on small fixed-wing aircraft (Hood *et al.* 1979; Hood 1981; Hood & Teskey 1989; Teskey *et al.* 1993). Later, heliborne gradiometer bird systems were deployed as simple vertical gradiometer systems (Hood & Teskey 1986) or as more advanced three or multi-sensor gradiometer systems, which measure longitudinal (in-line), transverse (cross-line) and vertical scalar field differences simultaneously (Scrivens *et al.* 2015).

Drone-towed magnetic surveying is rapidly becoming a competitive approach for providing high-resolution and consistent magnetic data, not only concerning mineral exploration and geological mapping (Heincke *et al.* 2019; Walter *et al.* 2019b, 2020; Døssing *et al.* 2021; Martelet *et al.* 2021), but also for mapping of subsurface pollution (Kolster & Døssing 2021a; Kolster *et al.* 2022) or archaeology (Balkov *et al.* 2019), where drone surveys may efficiently replace conventional ground-based survey techniques. Furthermore, for small to medium-sized surveys (<20–30 km²), the drone-towed approach may replace heliborne surveying and even achieve a higher data resolution while keeping the costs to a minimum (Døssing *et al.* 2021). The high data resolution can be achieved due to the possibility of acquiring data very close to the ground, even in steep terrain, and with a dense line spacing, following from the low cost per survey line. A majority of commercially available drone magnetic systems tend to focus on parameters like low weight, costs, and a high degree of user-friendliness. Commonly used drone magnetometer systems therefore often comprise one or more simple-to-operate fluxgate magnetometers, which may be mounted directly on the drone frame and, hence, under the direct influence of electromagnetic noise (Heincke *et al.* 2019; Jackisch *et al.* 2019; Le Maire *et al.* 2020). Alternatively, a towed scalar single-sensor system is deployed, either as a freely hanging magnetometer solution (Malehmir *et al.* 2017; Walter *et al.* 2019b) or as a single-sensor magnetometer bird (Døssing *et al.* 2021).

In order to replace high-resolution and high-quality heliborne gradiometry surveys, drone systems must provide data of comparable or superior resolution and quality (while maintaining an increase in net cost-benefit and survey flexibility). Parameters like the signal-to-noise ratio, positional precision and accuracy, and gradiometer setup are critical to meet such criteria. For example, a low noise level may be achieved by designing the drone gradiometer bird as a rigid system and placing the onboard magnetic sensors away from any electronics. Likewise, an onboard high-quality Global Navigation Satellite System and Inertial Measurement Unit (GNSS-IMU) can provide high positional accuracy and precision for the magnetometers. The drawback to these solutions is a net increase in system weight, price, and operational complexity. Nevertheless, meeting these criteria allows for the measurement of well-defined scalar field differences across multiple sensors (Kolster & Døssing 2021a,b; Kolster *et al.* 2022), but only along dynamic baselines, that is attitude variations are expected during flight (Fig. 1). For applications like mineral prospecting, where the geology of interest typically comprises well-defined structural trends, uniformly directed scalar field differences throughout the survey would be ideal. However, such measurements require the baseline to be aligned along a constant axis, which requires avoiding all attitude variations during flight. This study will denote such attitude variations deviating from the preferred axis of measurement as attitude deviations. The attitude deviations exhibited by the gradiometer bird system stem primarily from the pull of the drone, the resulting air drag, gravity, lift and weather effects, and to some degree (depending on the length of the towing cable) from downwash from the propellers of the drone. Typically, the aerodynamically designed bird will try to reach a stable configuration with respect to these forces, resulting in a semi-constant attitude deviation, not necessarily zero. However, multiple effects can momentarily disturb the stability and induce additional attitude deviations. These disturbances may come from sudden changes in the wind direction and speed (wind gusts), changes in the drone-bird dynamics or aerodynamic instability due to low horizontal speed (Walter *et al.* 2019a; Døssing *et al.* 2021; Kolster *et al.* 2022). Accumulation of these attitude deviations throughout a

gradiometry survey complicates data analysis, mainly if the survey has been conducted in a region with high-amplitude gradients.

The following presents a gradiometric equivalent source method (GESM) capable of predicting the uniformly directed scalar field differences from the measured scalar field differences. First, GESM is tested on simulated transverse horizontal difference (THD) responses to determine its accuracy in a controlled setting. Afterwards, GESM is showcased on data from an actual THD gradiometry survey conducted in Nautanen, Sweden. In addition, we examine how attitude deviations affect simulated THD responses and relate these attitude-induced THD responses to the stability of the bird.

2 METHOD

This section presents GESM and how it predicts the uniformly directed scalar field differences from the measured scalar field differences. The given data are the scalar field and position of the two sensors and the attitude of the bird. The scalar field data is denoted by \mathbf{d}_1 and \mathbf{d}_2 in units of nT for sensor 1 and 2 respectively. Likewise, the positional data are denoted by $\mathbf{P}_1 = [x_1 \ y_1 \ z_1]$ and $\mathbf{P}_2 = [x_2 \ y_2 \ z_2]$ in metres for sensor 1 and 2 respectively. Finally, the attitude data of the bird is denoted by α , β and γ in the yaw (with respect to the flight direction), pitch and roll rotations. The measured data from sensors 1 and 2 should be synchronized in time such that the i th row of both \mathbf{d}_1 and \mathbf{d}_2 corresponds to the same instant in time. We then define the measured data to be discreet measurements on the observational surface E. Likewise, we define new uniformly directed pseudo-sensor positions and their corresponding scalar field values to be discreet points on the continuation surface C. It is assumed that data at both of these surfaces are caused by surface magnetic polarization present on the dipole surface D. These surfaces are depicted in Fig. 2(a) along with the magnetic topography T. In short, GESM aims to take the positional data on E and construct the ideal pseudo-sensor positions on C. Then, estimate the surface magnetic polarization on D based on the measured data on E such that the uniformly directed scalar field differences on C can be estimated from D.

We start by defining the measured scalar field differences between sensors 1 and 2 present on E by

$$\Delta \mathbf{d}_{1,2} = (\mathbf{d}_1 - \mathbf{d}_2), \quad (1)$$

where $\Delta \mathbf{d}_{1,2}$ are the measured scalar field differences.

From the measured attitude and positional data on E, we can define the idealized pseudo-sensor positions \mathbf{P}_3 and \mathbf{P}_4 present on C as a function of the actual sensor positions:

$$\mathbf{P}_{3,i} = (P_{1,i} - P_{m,i}) \mathbf{R}(\alpha_i)^T \mathbf{R}(\beta_i)^T \mathbf{R}(\gamma_i)^T + P_{m,i} + s_i \quad (2)$$

$$\mathbf{P}_{4,i} = (P_{2,i} - P_{m,i}) \mathbf{R}(\alpha_i)^T \mathbf{R}(\beta_i)^T \mathbf{R}(\gamma_i)^T + P_{m,i} + s_i, \quad (3)$$

where $P_{1,i}$, $P_{2,i}$, $P_{3,i}$ and $P_{4,i}$ represent the i 'th row of \mathbf{P}_1 , \mathbf{P}_2 , \mathbf{P}_3 and \mathbf{P}_4 , respectively. $P_{m,i}$ is averaged positions of $P_{1,i}$ and $P_{2,i}$. The rotation matrices $\mathbf{R}(\alpha_i)$, $\mathbf{R}(\beta_i)$ and $\mathbf{R}(\gamma_i)$ rotates about the current heading, pitch and roll angles, respectively. s_i is an adjustment that vertically shifts sensor positions to the specified location on C. After these adjustments, the pseudo-sensor positions \mathbf{P}_3 and \mathbf{P}_4 will at one instant of time always be at the same height above topography and aligned orthogonal to the flight line direction.

We now formulate the continuation problem of transforming the measured scalar field on E to the pseudo-sensor positions on C. Following the derivation of Bhattacharyya & Chan (1977), we introduce the dipole surface D and formulate the continuation problem as

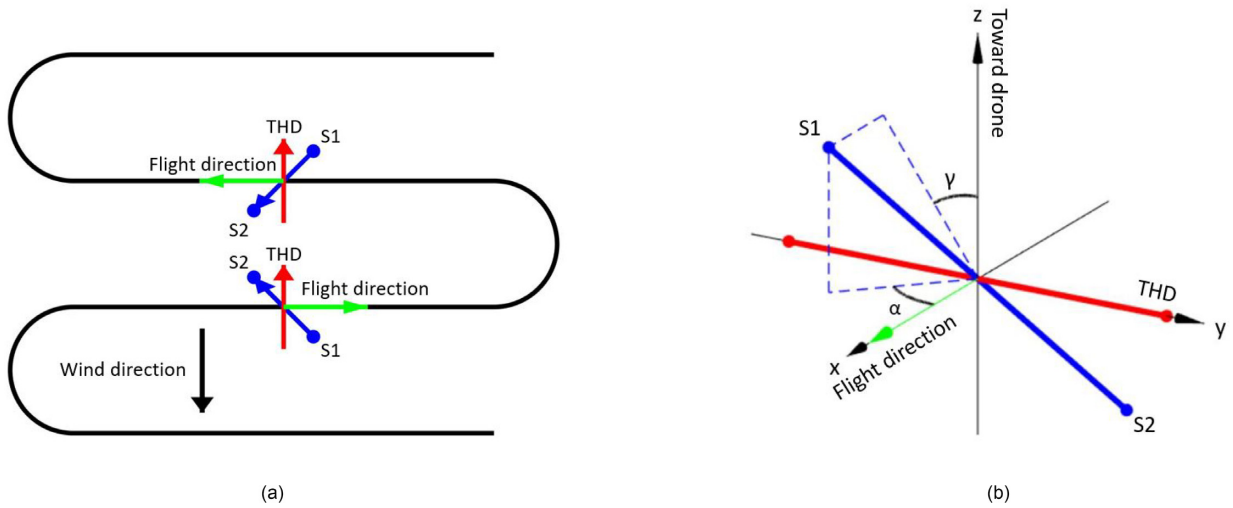


Figure 1. (a) Sketch showing the effect of the wind (black arrow) and pull from the drone (green arrow) on a custom-built gradiometry bird. S1 and S2 represent the two magnetometers in the bird system (blue arrow). The aerodynamically designed bird will align itself relative to the resulting wind resistance, causing changes in the birds’ attitude (yaw, roll and pitch). These attitude changes cause the misalignment in the transverse horizontal difference (THD) measured during the survey. The red arrow represents the desired uniformly directed THD. (b) Sketch of the misalignment between the measured THD and the ideal uniformly directed THD. The misalignment is quantified by a yaw rotation (α) followed by a roll rotation (γ). In this example, the pitch rotation will move the sensors equally along the x -direction and is therefore not sketched.

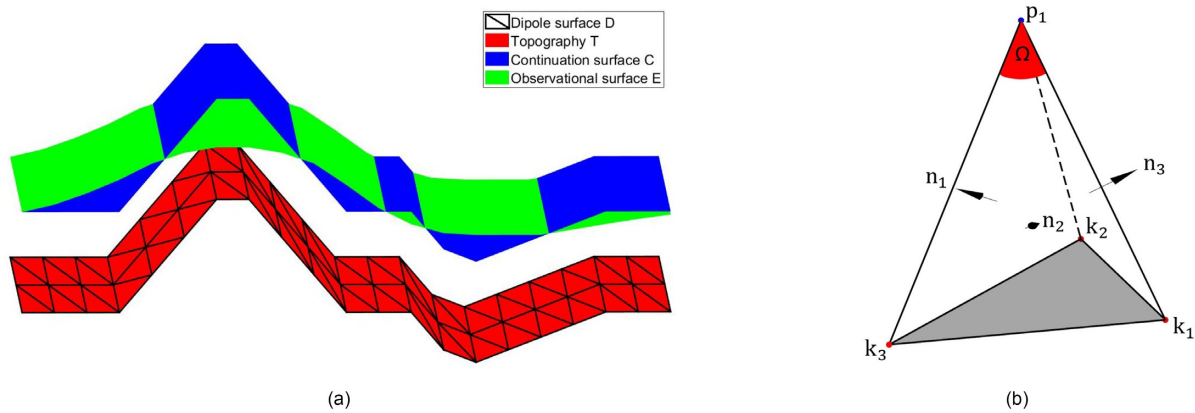


Figure 2. (a) Plot of the four surfaces: observational surface E, continuation surface C, dipole surface D and the topography surface T. D consist of triangular facets placed on T. (b) Plot showing a random data point p_1 and a random facet formed by k_1, k_2 and k_3 . These four coordinates form a tetrahedron where n_1, n_2 and n_3 are the normal vectors to the upper three planar elements. Ω represent the solid angle between the data point and the facet.

$$\begin{bmatrix} d_1 \\ d_2 \end{bmatrix} = -\frac{1}{4\pi} \int \int_D (\nabla_D \cdot \mathbf{u}) \mathbf{J} \left(\frac{\hat{\mathbf{n}} \cdot \mathbf{r}}{|\mathbf{r}|^3} \right) da \quad (4)$$

$$\begin{bmatrix} d_3 \\ d_4 \end{bmatrix} = -\frac{1}{4\pi} \int \int_D (\nabla_D \cdot \mathbf{u}) \mathbf{J} \left(\frac{\hat{\mathbf{n}} \cdot \mathbf{s}}{|\mathbf{s}|^3} \right) da, \quad (5)$$

where \mathbf{J} is the function describing the surface magnetic polarization present on D, and \mathbf{u} denotes the direction of the main magnetic field. da denotes an infinitesimal area on the dipole surface on which the magnetic polarization is constant both in magnitude and direction. $\hat{\mathbf{n}}$ is the outward directed normal vector to D. \mathbf{r} and \mathbf{s} are the distance vectors from a coordinate on E or C to the point of integration on D, respectively. \mathbf{d}_3 and \mathbf{d}_4 are the scalar fields present on C associated with the pseudo-sensor positions. The continuation problem is solved in two parts. First, the inverse problem of evaluating \mathbf{J} in eq. (4) based on measured data on E. Secondly, the forward problem evaluating \mathbf{d}_3 and \mathbf{d}_4 at the pseudo-sensor positions on C.

When \mathbf{d}_3 and \mathbf{d}_4 have been evaluated an equivalent expression to eq. (1) can be formulated for the uniformly directed scalar field

differences $\Delta \mathbf{d}_{3,4}$ on C as

$$\Delta \mathbf{d}_{3,4} = (\mathbf{d}_3 - \mathbf{d}_4). \quad (6)$$

Eqs (1)–(6) depict the basic formulation of GESM. However, in practice, the continuation problem cannot be solved analytically for complex configurations of the surface magnetic polarization.

2.1 Discretizing using planar polygons

The continuation problem requires integration over the entirety of the dipole surface. However, as proposed by Hansen & Miyazaki (1984) we can discretize D into planar facets and assign each facet a constant magnetic moment while fixing its polarization along the facet normal vector. This assumption simplifies the integration such that it can be done for arbitrarily shaped planar facets using the geometric integration method described by Ray (1984). Here, we discretize D into triangular facets and placing it such that it follows the local magnetic topography as depicted in Fig. 2(a). These

assumptions enable a finite facet discretization of the continuation problem, which for both eqs (4) and (5) can be written as

$$d_j = -\frac{1}{4\pi} \sum_i^M \mu_i \int_D \frac{\hat{\mathbf{n}}_i \cdot \mathbf{r}_{i,j}}{|\mathbf{r}_{i,j}|^3} d\mathbf{a}_i \quad (7)$$

$$= -\frac{1}{4\pi} \sum_i^M \mu_i \Omega_{i,j}, \quad (8)$$

where μ_i is the spatial gradient of the surface magnetic polarization in the direction of \mathbf{u} over the i th facet and d_j is the measured scalar-field from the j th data point. $\mathbf{r}_{i,j}$ and $\Omega_{i,j}$ are the radial distance and solid angle between the i th facet and the j th positional data point on either E or C. M is the total number of facets used in discretization.

To evaluate the solid angle geometrically, consider the i th measured data point \mathbf{p}_i and the three corners of the j th facet \mathbf{k}_1 , \mathbf{k}_2 and \mathbf{k}_3 . As depicted in Fig. 2(b), these four coordinates form a tetrahedron with three normal vectors from each of the three upper planes. These normal vectors can be defined as

$$\mathbf{n}_1 = (\mathbf{k}_1 - \mathbf{p}_i) \times (\mathbf{k}_1 - \mathbf{k}_2) \quad (9)$$

$$\mathbf{n}_2 = (\mathbf{k}_2 - \mathbf{p}_i) \times (\mathbf{k}_2 - \mathbf{k}_3) \quad (10)$$

$$\mathbf{n}_3 = (\mathbf{k}_3 - \mathbf{p}_i) \times (\mathbf{k}_3 - \mathbf{k}_1), \quad (11)$$

where \mathbf{n}_1 , \mathbf{n}_2 and \mathbf{n}_3 are the three normal vectors. The solid angle between j th triangular facet and the i th measured data point is the ratio of the area subtended by the facets unto the unit sphere placed at \mathbf{p}_i relative to its whole area (Salmon 1912). Following from Ray (1984) the solid angle can be calculated from the normal vectors of the three upper planes as

$$\Omega_{i,j} = -\pi + \sum_{i=1}^2 \sum_{j=2}^3 \delta_{i,j} \arccos \left(-\frac{\mathbf{n}_i \cdot \mathbf{n}_j}{|\mathbf{n}_i| |\mathbf{n}_j|} \right), \quad (12)$$

where $\delta_{i,j} = 1$ when $i \neq j$ and $\delta_{i,j} = 0$ when $i = j$. The finite facet discretization of the continuation problem can now be obtained by inserting eq. (12) into eq. (8).

2.2 Stable solution to the continuation problem

Until now, we have only discretized the continuation problem. To solve the continuation problem we modify it slightly such that it relates μ directly to the sensor differences $\Delta \mathbf{d}$. This can be done by inserting eq. (8) into eq. (1) or (6) resulting in this forward problem:

$$\Delta \mathbf{d} = -\frac{1}{4\pi} (\mathbf{\Omega}_{S1} - \mathbf{\Omega}_{S2}) \boldsymbol{\mu} + \boldsymbol{\epsilon} \quad (13)$$

$$= \mathbf{G} \boldsymbol{\mu} + \boldsymbol{\epsilon}, \quad (14)$$

where $\mathbf{\Omega}_{S1}$ and $\mathbf{\Omega}_{S2}$ are matrices containing the solid angles subtended by all facets unto all positions of sensors 1 and 2, respectively. $\Delta \mathbf{d}$ is the scalar field differences, which can describe either $\Delta \mathbf{d}_{1,2}$ or $\Delta \mathbf{d}_{3,4}$ depending on the positional data on E or C used to construct $\mathbf{\Omega}_1$ and $\mathbf{\Omega}_2$. \mathbf{G} is the kernel matrix of this forward problem. $\boldsymbol{\epsilon}$ is a noise term and describes any measurements noise and discretization errors.

The inverse problem of estimation $\boldsymbol{\mu}$ given the measurements of $\Delta \mathbf{d}_{1,2}$ in eq. (13) is often ill-posed, and naive solutions of $\boldsymbol{\mu}$ can be extremely unstable. Instabilities in $\boldsymbol{\mu}$ can cause an erroneous continuation and interpolation of $\Delta \mathbf{d}_{3,4}$ on the continuation surface. Therefore, we enforce stability by minimizing the spatial gradient of $\boldsymbol{\mu}$ across different facets in addition to the data residual. This minimization effectively applies local smoothness constraint across neighbouring facet of $\boldsymbol{\mu}$.

The spatial gradient of $\boldsymbol{\mu}$ is estimated using the finite-difference approximation. Consider a single triangular facet containing μ_j , and an associated facet-circumference (f) assembled by its three side lengths. Then the neighbouring three facets (μ_{j+1} , μ_{j+2} and μ_{j+3}) each share one side lengths with μ_j . The gradient at μ_j is then approximated from the neighbouring facets as

$$\frac{a}{f} \mu_{j+1} + \frac{b}{f} \mu_{j+2} + \frac{c}{f} \mu_{j+3} - \mu_j = q \quad (15)$$

where a , b and c are the three sides of the j th facet and q is the estimated gradient at μ_j . Eq. (15) can now be generalized into a matrix–vector system to encompass all facets simultaneously:

$$\mathbf{L} \boldsymbol{\mu} = \mathbf{q}, \quad (16)$$

where \mathbf{L} is the desired difference matrix and \mathbf{q} is the estimated gradient across all facets.

The inverse problem of estimating $\boldsymbol{\mu}$ in eq. (13) given the smoothness constraint can be formalized as a Tikhonov regularized least-squares problem, which can be expressed as

$$\boldsymbol{\mu} = (\mathbf{G}^T \mathbf{G} + \lambda^2 \mathbf{L}^T \mathbf{L})^{-1} \mathbf{G}^T \Delta \mathbf{d}_{1,2}, \quad (17)$$

where the first term of eq. (17) quantifies the data residual while the second term quantifies the spatial gradient of $\boldsymbol{\mu}$. λ^2 is the regularization parameter and controls the relative importance of the smoothness constraint and determined using an L-curve method (Aster *et al.* 2018). Now the modified discretized continuation problem can be solved by evaluating $\boldsymbol{\mu}$ in eq. (17) followed by evaluating $\Delta \mathbf{d}_{3,4}$ from eq. (13).

To summarize GESM, we start applying the positional adjustments to \mathbf{P}_1 and \mathbf{P}_2 on E through eqs (2) and (3) to obtain \mathbf{P}_3 and \mathbf{P}_4 on C. Then, we place the dipole surface on the local magnetic topography and apply the finite facet discretization to the continuation problem. The modified discretized continuation problem is now solved by evaluating $\boldsymbol{\mu}$ in eq. (17) given $\Delta \mathbf{d}_{1,2}$ and then evaluating $\Delta \mathbf{d}_{3,4}$ from eq. (13) given $\boldsymbol{\mu}$.

3 DATA ACQUISITION

The Nautanen survey was planned and conducted for the purpose of mineral exploration. Mineral exploration requires high-resolution and high-quality data. Therefore, several steps were made to achieve this, for example deploying a custom-made gradiometer bird, draping the topography and a line spacing equal to the flight height.

The bird incorporates a Novatel SPAN GNSS Inertial Navigation System (GNSS-INS) and two QuSpin Total-Field Magnetometers (QTFM). The GNSS-INS system is comprised of a SPAN GNSS receiver, sampling at 1 Hz, and a SPAN Inertial Measurement Unit (IMU), sampling at 10 Hz. All GNSS, inertial, and gyro data were post-processed in the Novatel Inertial Explorer software, utilizing its manufacturer-specified parameters for the multi-pass Kalman filter. The QTFM is a lightweight (18 g per sensor) rubidium-based optically pumped magnetometer, sampling at ~ 203 Hz with a sensitivity of < 1 pT Hz $^{-1/2}$. The QTFM has dead zones in the equatorial plane ($\pm 7^\circ$), which can easily be avoided by calibrating the sensor before surveying. In total, the bird weighs ~ 4 kg enabling a flight time of ~ 12 – 14 min using the Wind 4 UAV from DJI.

The Nautanen survey was planned with these specifications: 30 m line spacing, 30 m topography-draped (altitude of bird), towing cable length of 10 m (vertical separation between the drone and the bird), set horizontal drone speed of 11 m s $^{-1}$, maximum vertical ascending and descending speed of 4 m s $^{-1}$, and a 2.05 m horizontal gradiometer baseline. With these specifications, the Nautanen

survey was conducted on the sixth and seventh of May 2019. Numbered from North to South (see Fig. 3), flight lines 15–33 were flown late afternoon of survey day one, while flight lines 1–14 and 34–38 were flown in the morning to early afternoon of survey day two. In addition, we rotated and translated the positional data such that flight lines are flown approximately along the x -axis, and the centre of the survey is in the coordinates system's origin. Weather records from the sixth and seventh of May showed a 3–4 m s^{-1} western wind on survey day one, and survey day two showed 0–1 m s^{-1} with scattered wind direction in the morning while early afternoon showed 3 m s^{-1} eastern winds.

In the pre-processing, we downsampled to 1 measurement every 2 m, corresponding to ~ 5.5 Hz. We deemed this downsampling appropriate for a geological survey. This downsampling also significantly reduces the inversion and forward calculation time of GESM. However, we would not recommend downsampling to this degree for surveys for smaller shallow sources, for example UXO detection. The Nautanen survey presented in this study has not been levelled or micro-levelled beforehand.

4 RESULTS

This section presents the results of GESM when applied to the Nautanen THD survey to correct the attitude deviations exhibited by the bird. First, we present the actual attitude data and assess the in-flight stability of the bird. Secondly, we investigate how attitude deviations affect the measured THD in a synthetic example and test the accuracy of GESM. Finally, we showcase GESM when applied to the actual THD from the Nautanen survey.

4.1 In-flight stability and attitude deviations

Fig. 3 visualizes the in-flight stability of the bird during the Nautanen survey as highlighted by the recorded attitude data and their dependency on the horizontal speed of the bird. The data are shown on top of a contour plot of the local topography. Fig. 3(a) shows that the steepness of the topography limits the horizontal speed of the drone-bird system; an effect visualized by the blue colour observed primarily when the drone ascends or descends the \sim N–S trending hill in the western part of the survey. This decreased in horizontal speed is particularly well visualized in Fig. 3(b), which depicts the vertical versus horizontal speed of the drone-bird system. As seen, the drone-bird system can maintain a horizontal speed of 11 m s^{-1} as long as the vertical velocity is below 3 m s^{-1} . Over steep topography, the horizontal speed drops to 4–10 m s^{-1} while the vertical velocity increases to 4 m s^{-1} limited by the set ascending/descending rate.

Depicted in Fig. 3(c) is the angle between the measured and desired heading of the bird, denoting the yaw deviations. The yaw deviations show sign shifts from line to line combined with large oscillations at the start of new flight lines. In Figs 3(e) and (g) is the measured roll and pitch angles of the bird, denoting the roll and pitch deviations. The roll deviations also show oscillations at the start of and throughout flight lines, whereas the pitch deviations show mostly positive values with higher amplitude in the western part. Note that in a THD survey, the roll and yaw deviations affect the alignment of the baseline in the vertical plane and the horizontal plane, respectively, while the pitch deviation moves the sensors equally and will not propagate into the measured THD.

The scatter plots in Fig. 3 provide insight into the in-flight stability of the bird during the Nautanen survey. The dense regions

of the scatter plots indicate that the bird's attitude is relatively stable around preferred orientation. The vertical velocity and the roll deviations showcase a single mode distribution centred at 0 m s^{-1} and 0°, respectively. The yaw deviations showcase a clearly defined bimodal distribution centred at -11° and 15° . Finally, the pitch deviations showcase a distribution with two distinct but overlapping modes at 1° and 7° . The sparse regions indicate that the bird's attitude is unpredictable and seen primarily when the horizontal speed is lower than 10 m s^{-1} . However, extreme roll and pitch deviations can also be observed at optimal horizontal flight speed. From these distributions, we define stable and unstable flight phases. Stable flight phases happen when the bird exhibits vertical speeds and attitude deviations close to the modes, whereas unstable flight phases happen in the sparse region.

4.2 Correction of attitude deviations

We verify pseudo-sensor positions created by eqs (2) and (3) by showing the axial differences between the two sensors positions before and after yaw and roll adjustments in Fig. 4. In the coordinates system defined, roll deviation will primarily result in z -axis differences, while yaw deviations will primarily result in x -axis differences. The implications are that the sensor positions resulting in uniformly directed THD will share z - and x coordinates, while the y -coordinate differences reflect the THD baseline. The measured sensor positions show that the z -axis differences vary from -0.5 to 0.5 m. The x -axis differences showcase two modes: one centred around 0.5 m differences and another centred around -0.5 m difference. The absolute y -axis differences vary from 0.5 to 2.05 m. For the pseudo-sensor positions, the z -axis differences now only range from -0.01 to 0.01 m, the x -axis differences range from -0.1 to 0.1 m, and the absolute y -axis differences range from 2.04 to 2.06 m. As indicated by the statistics and histograms, there are still some minor nonadjustable attitude deviations corresponding to absolute yaw and roll deviations of 8° and 2° , respectively.

4.3 Results from the synthetic example

The synthetic example consists of synthetic THD responses created from magnetized prisms overlain by measured and pseudo-sensor positions from the Nautanen survey (Figs 3 and 4). These THD responses are assumed to be discrete measurements from four surfaces: The observation surface E contains the measured sensor positions and three continuation surfaces (C1, C2 and C3) contains the pseudo-sensor positions (eqs 2 and 3). C1 only have yaw adjustments, C2 have both roll and yaw adjustments and C3 have roll, yaw, and topography adjustments. Here the topography adjustment vertically shifts the sensor positions to a smooth continuation surface. We added 2 nT Gaussian noise to the THD on E to simulate observational noise. The simulated THD on the four surfaces are depicted in column 1 in Fig. 5. The goal now is to apply GESM to the THD on E and compare the result to the THD on the continuation surfaces.

GESM was initialized by placing D on the topography from the Nautanen area. We ensured that D extended outside the edge of E by at least 30 m, that is equal to the survey altitude. Next, the finite facet discretization was done by dividing D into 8000 equal-sized triangular facets. The results of GESM, when applied to the THD on E and its predicted THD response at the measured and pseudo-sensor positions comprising the four surfaces, are depicted in column 2 in Fig. 5. Here, λ^2 was optimized using the L-curve

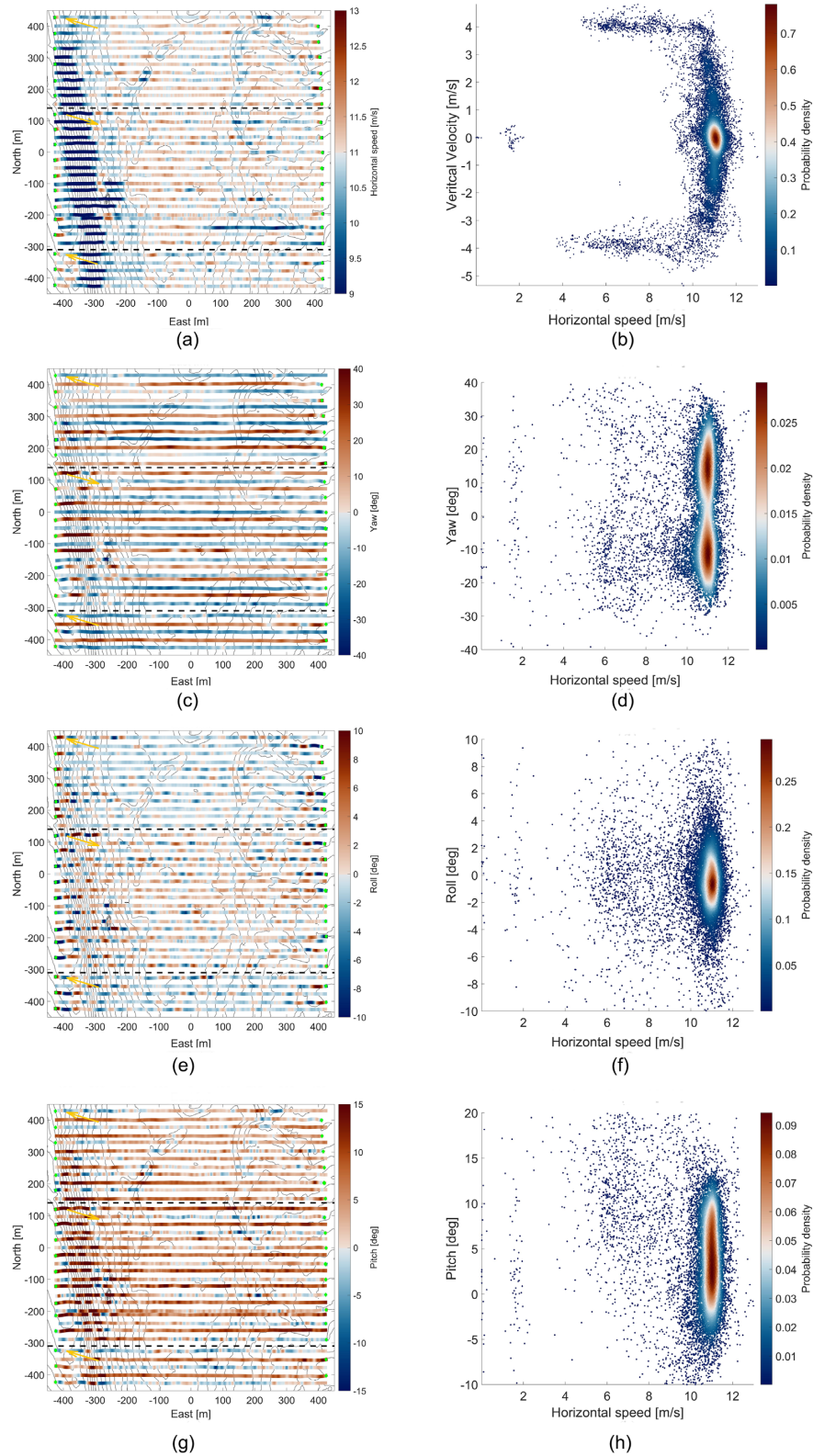


Figure 3. Visualization of the in-flight stability of the bird. (a, c, e and g) The horizontal speed, yaw, roll and pitch deviations of the bird regarding its location and draped topography, respectively. The topography contour lines highlight a 5 m difference in elevation. The dotted lines separates the survey days. Yellow arrows indicate the major wind direction of the survey day. (b, d, f and h) The vertical velocity, yaw, roll and pitch deviations regarding horizontal speed, respectively.

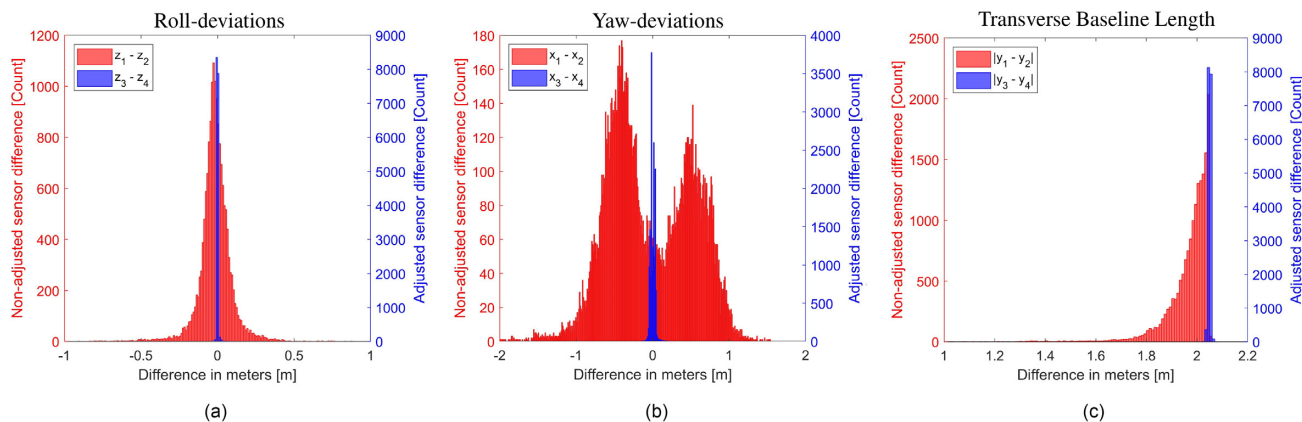


Figure 4. Axial differences for the measured sensor positions (red histograms) and pseudo-sensor positions (blue histograms). (a) Histogram of the z -axis differences between sensor positions, which indicates roll-deviations. (b) Histogram of x -axis differences between sensor positions, which indicates yaw deviations. (c) Histogram of absolute y -axis differences between sensor positions, which indicates the baseline length along the desired direction. The plots show that the sensor positions on C2 showcase almost no attitude deviations after the attitude adjustments.

method giving $\lambda_{opt} = 0.1450$. Finally, the residuals between the simulated THD and predicted THD using GESM are depicted in column 3 in Fig. 5.

Fig. 5 showcases how attitude and topography adjustments affect simulated THD responses and whether GESM can accurately predict the simulate THD. A comparison of Figs 5(a) and (d) shows that the yaw adjustment primarily removes line-to-line striping in the THD maps. Similarly, Figs 5(d) and (g) show that also adding the roll adjustment removes short-wavelength signals in the THD maps. Finally, Figs 5(g) and (i) show that the topography adjustment result in slightly smoother THD maps. Note that the differences between Figs 5(a) and (g) result only from the attitude deviations. Ideally, the simulated THD on C3 should be a completely smooth surface and the signals still present stem from the minor non-adjustable attitude deviations.

A visual comparison between the simulated THD and predicted THD (columns 1 and 2 in Fig. 5) shows overall a good agreement between them. However, on the surfaces C2 and C3, the predicted THD maps seem a bit more rugged than the corresponding simulated THD maps. The residuals in column 3 in Fig. 5 showcase the accuracy of GESM on all four surfaces. The residuals indicate a slight correlation in the cross survey direction. However, the residuals on C1, C2 and C3 show less correlation in the cross survey direction and more correlated locally, likely the cause of the ruggedness observed in the predicted THD maps. The root mean square of the residuals (RMS-residuals) on E was 1.6 nT, slightly lower than the applied 2 nT Gaussian noise. The three continuation surfaces also used as references had RMS-residuals all below 1 nT.

4.4 GESM on actual gradiometry data

The actual gradiometry survey from Nautanen had significant attitude deviations but also a non-optimal draping of the topography. Therefore, we define new pseudo-sensor positions with yaw, roll and topography adjustments placed on a continuation surface C. GESM was initialized and constructed identically to the synthetic example but with $\lambda_{opt} = 0.0074[\text{nT}]^{-1}$. The result of GESM, when applied to measured THD from Nautanen, was obtained by predicting the THD response at the pseudo-sensor positions on C.

Fig. 6(a) shows the measured THD from Nautanen, and both the yaw- and roll-induced line-to-line striping and short-wavelength signals are apparent. Fig. 6(b) shows the predicted THD on C, and

its seemingly free of the yaw- and roll-induced signals. In addition, previously hidden small-amplitude anomalies have been resolved. In this actual gradiometry example, we achieved a RMS residual of 0.72nT between the measured THD and predicted THD on E.

Fig. 7 shows the measured THD and the predicted THD using GESM on C and E from two profiles flown east–west. Additionally, Fig. 7 shows the yaw and roll deviations, transverse baseline length, and horizontal velocity inherent to the measured and pseudo-sensor positions. Fortunately, this line was flown twice at different times during survey day 2; therefore, this example directly shows the effect the attitude-induced THD responses. Fig. 7(c) shows that when the yaw deviations differ significantly between the two lines, so do the measured THD. Fig. 7(d) shows that the roll deviations only slightly affect the measured THD, with their magnitude greatest at the beginning and end of the flight lines. In the pseudo-sensor positions, we still see small peaks in its attitude deviations, an artefact from the nonadjustable attitude deviations from Fig. 4. Fig. 7(e) shows the length of the transverse baseline was more varied along line 11, whereas for line 10 it was much more stable. Flight line 11 also has more abrupt velocity changes, and both lines display a drop in horizontal velocity over the hills in the eastern parts of the survey (see Fig. 7f). Overall, more yaw and roll deviations are present on flight line 11 than on flight line 10. Additionally, yaw deviations can add 10 nT to the measured THD in high gradient areas, whereas roll deviations add significantly less. The predicted THD on E shows a good but not perfect fit to the measured THD on flight line 10 and 11. As expected, the predicted THD on C is almost identical for the two identically flown flight lines.

5 DISCUSSION

5.1 Attitude deviations in stable flight

The measured attitude deviations reflect whether the bird was in a stable or unstable flight phase. The stable flight phases were determined from the modes of the distributions in Fig. 3, which indicated that the bird had two in-flight stability configurations. The two stability configurations are related to the two primarily flight directions and the horizontal velocity of the bird along the lines relative to the local wind velocity. As showcased by Fig. 1, we expect the bird to exhibit constant directional dependent yaw deviations in a constant transverse wind. Likewise, in upwind and downwind, we expect

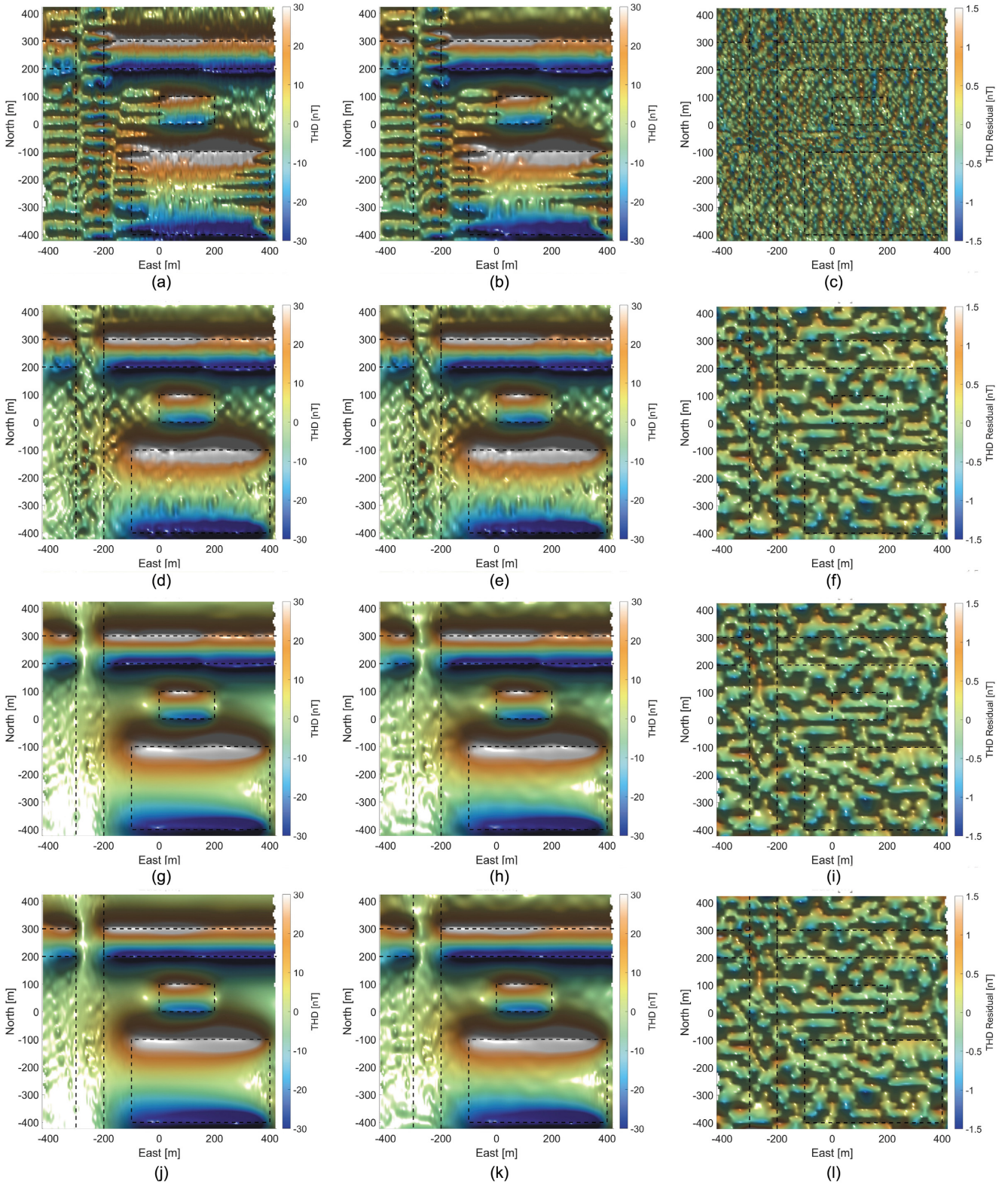


Figure 5. Results of the synthetic example. Row 1 to 4 represent the results of the analysis for each of the four surfaces E, C1, C2, C4, where column 1 shows the simulated THD, column 2 shows the predicted THD using GESM and column 3 shows the residuals between the simulated THD and predicted THD. All THD maps were created using a cubic spline bidirectionally interpolation algorithm, while the residuals maps were created using a linear interpolation algorithm. All maps were illuminated from the south. The dotted black lines show the outline of the magnetic prisms.

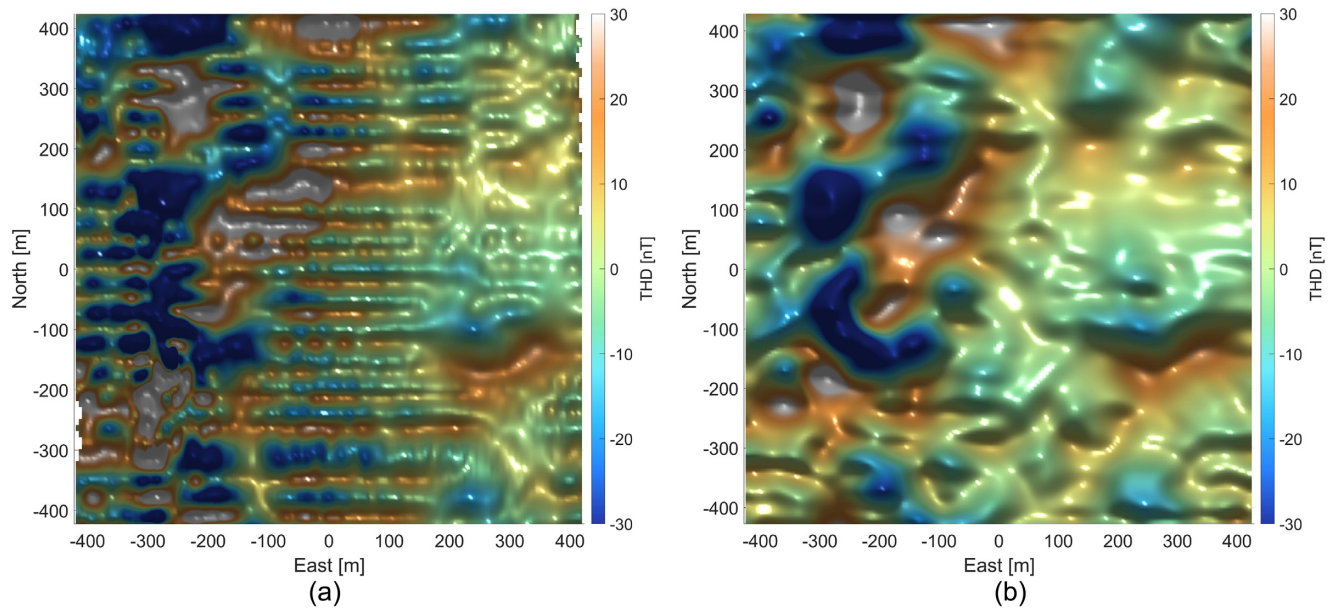


Figure 6. Results of applying GESM to the measured THD from Nautanen, Sweden, in the rotated and translated coordinate system. (a) The measured THD from Nautanen interpolated using a cubic spline bidirectionally interpolation algorithm. (b) Result of GESM when applied to the measured THD from Nautanen and its predicted THD response at C, that is pseudo-sensor positions placed in a grid formation always 2.05 m apart and uniformly directed. Both maps were interpolated to the same 5x5 m grid and illuminated from the Southern direction.

directional dependent pitch deviations with magnitude determined by the relative horizontal velocity in regard to the wind velocity. Lastly, we expect the distribution of the roll deviations under stable flight to be centred closely around 0 degree. In stable flight, we do not expect the drone to move suddenly in the transverse direction; therefore, attitude deviations from stable flight mainly results from the bird rotating about its own axes.

We see the directional-dependent yaw deviations as the line-to-line shifts in Fig. 3(c) and as the bimodal distributions in Figs 3(d) and 4(b). Likewise, Figs 3(g) and (h) show the directional dependent pitch deviations. Here, the line-to-line shifts are less pronounced, and the modes of the bimodal distributions are less separated. In perfect calm conditions with no winds, the bimodal distributions would collapse into single-mode distributions, as no directional-dependent attitude deviation is expected in this case. If we instead had stronger winds, we would expect the distance between the modes to increase, causing a larger difference in attitude deviation between the two flight directions. In addition, a change in the wind direction from western to eastern, as seen between the two survey days, would cause the modes of the distributions to switch place, thereby causing a sign-change in the directional dependent yaw and pitch deviations of flight lines flown in the same direction. In Fig. 3(c), we see this effect as neighbouring flight lines (flown in opposite directions but on separate days) both having positive/negative attitude deviations.

During a full-day survey, the wind's transverse and longitudinal velocity components will typically change, causing the bird to enter many stable configurations generating the bimodal distributions observed in the yaw and pitch deviations. However, based on the magnitude of these attitude deviations, our bird seems more sensitive to transversely directed wind effects than longitudinally directed wind effects. This sensitivity likely stems from the fact that the drone travels 11 m s^{-1} in its longitudinal direction (significantly faster than the maximum upwind and downwind speed of 3 m

s^{-1}), whereas the drone has no travelling velocity in the transverse direction.

5.2 Attitude deviations in unstable flight

The unstable flight phase for the bird was determined to primarily occur when the combination of the wind speed and forward flight speed fell below 11 m s^{-1} , that is the relative airspeed flowing past the bird needs to be steadily kept above 11 m s^{-1} to maintain stable flight. On Fig. 7(f), line 11 has more sporadic movement down the flight lines and also has much higher attitude deviations than line 10. Therefore, below this 11 m s^{-1} speed threshold, the bird is less aerodynamically stable, resulting in an oscillation phase in attitude deviations characterized by a decay rate and a frequency. We can identify two types of oscillation patterns along the flight line in Figs 3(c), (g) and (e). One pattern is at the beginning of a new flight line, while the other seems to occur randomly during flight. Walter *et al.* (2019a) analysed the oscillation frequency for a single sensor system and found the main oscillation frequencies of the system to be in the range 0.2–0.5 Hz. They determined these oscillations to primarily stem from the pendulum-like setup of the drone/bird system. For our custom-built gradiometry setup, we find the main oscillation frequencies of the system to be in the range 0.1–1 Hz, that is a wider span than the frequencies of Walter *et al.* (2019a), which could be consistent with our longer towing cable (10 m) in the pendulum-like setup.

We can now identify that the first oscillation pattern is generated by shifting flight lines which can induce pendulum-like motions in the drone-bird setup. Likewise, the second oscillation pattern is likely due to wind gusts pushing the drone-bird setup into a pendulum-like motion. Unlike the stable flight phase, where attitude deviations result from the bird's rotation about its own axis, attitude deviations from the unstable flight phase can also result from the complex pendulum-like drone-bird setup.

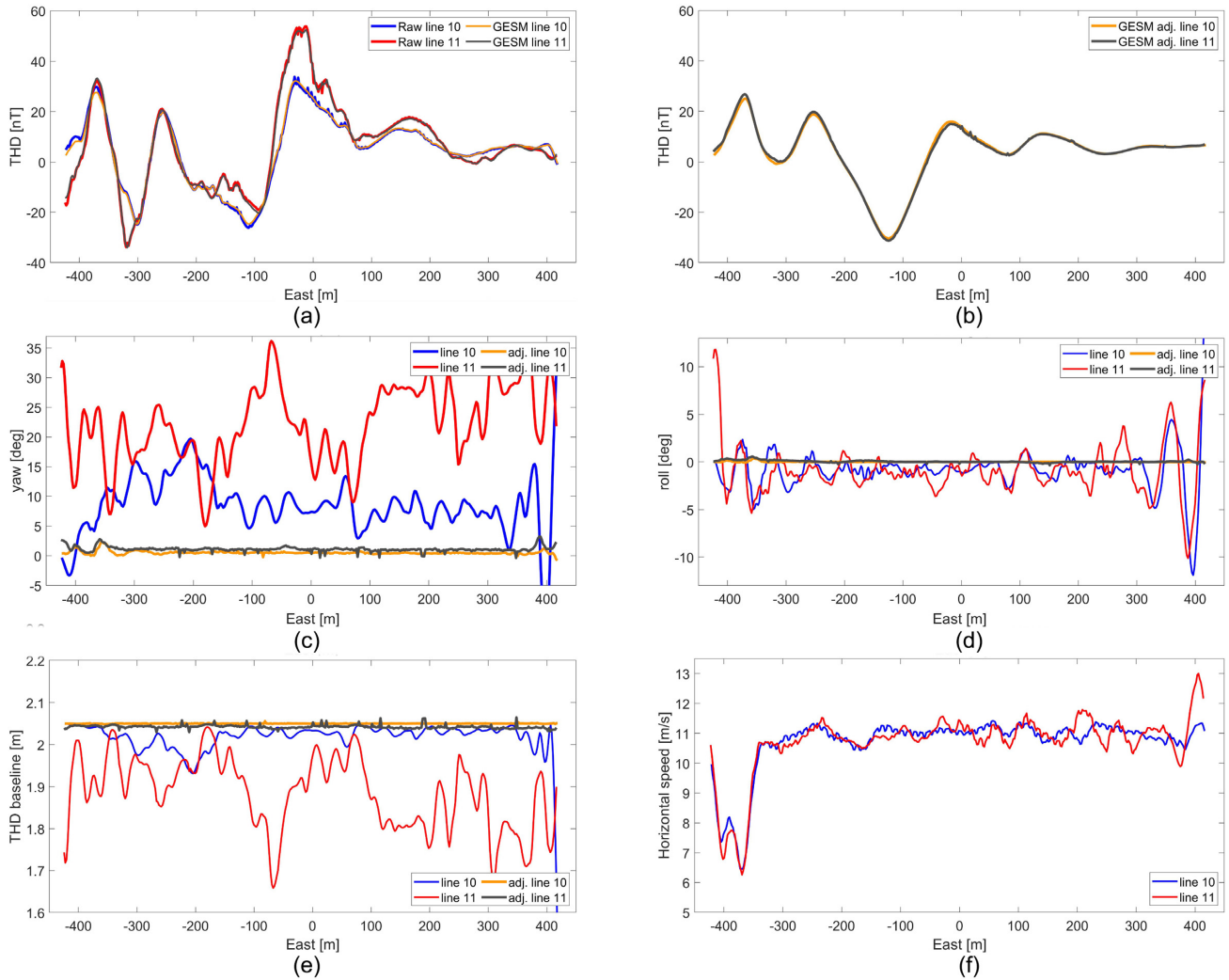


Figure 7. Measured and GESM adjusted data along two flight lines (line 10 and 11) flown at a different times but along the same flight path. The red and blue lines show the measured data before applying GESM, and the yellow and black lines show GESM adjusted data. (a) The measured and predicted THD at the measured sensor positions. (b) The predicted THD at the adjusted sensor positions. (c) The yaw deviations of the measured and adjusted sensor positions. (d) The roll deviations of the measured and adjusted sensor positions. (e) The transverse baseline length of the measured and adjusted sensor positions. (f) The measured vertical velocity.

5.3 The effect of attitude deviations on the measured THD

The purpose of a THD measurement is to quantify the scalar field variation along the transverse axes. However, the stability of the gradiometer bird will affect the THD response by rotating the baseline (\mathbf{b}) from the desired transverse orientation to a random orientation. This random orientation contaminates the THD responses along \mathbf{b} with scalar field variations along the longitudinal and vertical spatial axes. We can infer the orientation of \mathbf{b} from the histograms in Fig. 4 and relate \mathbf{b} to its THD response by comparing the simulated THD maps in Figs 5(a), (d) and (g).

In stable flight, the orientation of the baseline can be determined from the modes of the distributions in Fig. 4(b) as $\mathbf{b}_s = [\pm 0.5 \ 2 \ 0]$ which correspond to the bird exhibiting a yaw deviation of ± 14.1 degrees. The components of \mathbf{b}_s is determined from the fact that $\|\mathbf{b}\| = 2.05$ and knowing the x -, y - and z -component from the histograms. In this case, the actual baseline length in the transverse direction is only 2 m, but ± 0.5 m in the longitudinal direction. As this effect shifts sign based on flight direction, it effectively induces striping in the THD due to the longitudinal scalar field variations,

which is in agreement with the THD maps on C1 in Fig. 5(d) that shows that yaw adjustment is sufficient to remove the line-to line striping.

In unstable flight, the orientation of the baseline \mathbf{b}_{us} oscillates, resulting in yaw and roll deviations that can exceed $\pm 35^\circ$ and $\pm 10^\circ$, respectively, decaying back to \mathbf{b}_s . The baseline vector in this scenario can oscillates in between and even exceed $\mathbf{b}_{us} = [\pm 1.16 \ 1.65 \pm 0.35]$, also confirmed as possible configurations from Fig. 4. This oscillation result in THD responses along \mathbf{b}_{us} that are essentially a random measurement of the scalar field variation along the transverse, longitudinal and vertical axes. As the unstable phase is only temporary, the THD response along \mathbf{b}_{us} dampens and returns to the stable THD response along \mathbf{b}_s . This effect produces short spatial wavelength signals in the THD, which agrees with the THD maps on C2 in Fig. 5(g), which show that both roll and yaw adjustments are needed to remove the short-wavelength signals.

The magnitude of the THD response along either \mathbf{b}_s and \mathbf{b}_{us} depends not only on the bird's orientation but also on the local gradients in the scalar field. For example, In a high-gradient area in

the Nautanen survey, a change in yaw deviation of 20° can change the measured THD by 20 nT (Fig. 7). Furthermore, comparing Figs 5(a), (d) and (g) shows that attitude-induced THD responses magnifies in the vicinity of the magnetic prisms, that is in high-gradient areas. Hence, accumulations of attitude deviations in a high gradient area can pose severe problems for the interpretation of geology, particularly for relatively low-speed surveys.

5.4 Accuracy of GESM

In the synthetic example, an accuracy analysis of GESM based on the residuals on the observational surface and the three continuation surfaces shows a good fit and an acceptable RMS-residual (column 3 in Fig. 5). The residuals on the observation surface show some local correlation. However, the correlation area is relatively small but slightly tends to be extended in the transverse direction. The residuals on the continuation surfaces also show a local correlation but with a larger correlation area, extending in the longitudinal direction. Additionally, the residuals on the correlation surfaces are almost entirely identical. This suggests a bias in GESM to replicate the synthetic model exactly. This bias is likely an artefact of overfitting the noise and inefficiencies in the modelling.

Fig. 7 shows that GESM can fit the measured data, although not perfectly, and produce consistent results for flight lines flown along the same flight path. However, the GESM predicted THD for line 11 has peaks at 0 m east due to nonadjustable attitude deviations. We suspect these are an artefact of the Kalman filter used to process the GNSS and IMU data. Generally, for both the simulated and measured THD responses (Figs 5 and 6), GESM removed both the line-to-line striping and the short-wavelength signals caused by the attitude deviations exhibited by the bird. The synthetic example consists of THD responses from large magnetic prisms is clearly best represented by the THD maps on C3 shown in Fig. 5(i), which indicates that GESM allows for a more accurate interpretation of the underlying sources. The actual example, Fig. 6(b) reveals many smaller anomaly signals previously hidden due to attitude deviations. However, some of these anomaly signals could be artefacts due to overfitting or inefficiencies in the modelling. The short wavelengths comprising these smaller anomalies could potentially overlap with the short wavelengths induced by attitude deviations. Therefore, attitude correction using low-pass filters, as sometimes done in single sensor surveys, could potentially remove signals from these small anomalies. In contrast, an attitude-informed compensation method such as GESM, targets only the attitude-induced THD responses and preserves the smaller anomalies.

GESM removes attitude-induced responses by interpolating and continuing the measured scalar differences using equivalent sources to new idealized pseudo-sensor positions free of any attitude deviations (after yaw, roll and topography adjustments). The accuracy of the interpolation and continuation depends on the fitted dipole surface, which ultimately depends on the quality of the measured data. Therefore, high precision of the GNSS and IMU measurements is considered a prerequisite for GESM, especially for surveying high gradient areas where minor positional magnetometers can lead to significant errors in the measured THD. In addition, any heading errors, biases on the magnetometers or discretization errors can introduce erroneous signals into the continuation field. Worst case, these erroneous signals cause the estimation of μ to be unstable as a result of the sensitivity of the kernel matrix \mathbf{G} . Additionally, \mathbf{G} is sensitive to the placement of the dipole surface in regards to the observational surface. Placing the dipole surface away from the

observational surface produces a smoother continuation field, while placing it closer produces a more rugged continuation field. Hansen & Miyazaki (1984) argued that the dipole surface should be placed on or close to the observational surface and discretized such that each data point has a facet below it, resulting in \mathbf{G} being diagonal dominant. However, based on our synthetic test, we found that this approach, combined with a rugged observational surface, scattered data and a small continuation length, resulted in an erroneous field continuation. Instead, we placed the dipole surface in the vicinity of the dominant magnetic source or at a maximum distance of twice the flight line spacing. This placement improves our continuation accuracy but also increases the condition number of \mathbf{G} . In the future, it might be beneficial to parametrize μ as harmonic functions with an approach similar to Fedi *et al.* (1999), which could improve the condition number of \mathbf{G} and enable faster inversion of larger data sets. Due to these sensitivity considerations, we recommend some user agency regarding the placement, discretization and fitting of dipole surface to achieve the best possible results utilizing GESM.

6 CONCLUSION

Our study demonstrates that the in-flight stability of a drone-towed gradiometer system can significantly impact the measured THDs. Depending on wind conditions, the drone/gradiometer system dynamics and the local magnetic gradient, this impact can be characterized by line-to-line striping and/or short-wavelength oscillations in the THD maps.

We present a gradiometric equivalent source method (GESM) to remove attitude-induced responses from measured scalar field differences. The method removes these attitude-induced responses by interpolating and continuing the measured scalar field differences from their measured positions to new uniformly directed pseudo-positions. GESM was successfully applied to synthetic and actual THD responses, showcasing that the method removes attitude-induced THD responses with satisfactory accuracy. Furthermore, the resulting THD maps demonstrate an improved continuity of anomalies, thereby facilitating a more accurate interpretation of the geology of interest.

A prerequisite for applying GESM is high-quality onboard GNSS-IMU system enabling well-defined sensor positions. This precise positional information enables GESM to distinguish between attitude-induced anomalies and genuine anomalies from magnetic sources. The method relies on solving an ill-posed continuation problem and will therefore be sensitive to data error and the placement and discretization of the dipole surface. To balance these sensitivity issues, we recommend some user agency in determining the dipole surface so that the interpolation and continuation to these pseudo-positions are as accurate as possible. Nevertheless, the results suggest that including GESM in the processing of drone-towed gradiometry surveys, given precise positional information is available, ensures high-quality geological interpretation even when surveying in windy conditions or in high-gradient areas.

ACKNOWLEDGMENT

We would like to thank Eduardo da Silva, Vamsi Krishna, Johannes Linde and Mahendra Pal for aiding in fieldwork and data collection during this study.

DATA AVAILABILITY

Additional publications using the data are underway. As such, data will only be made publicly available after these publications.

REFERENCES

- Aster, R.C., Borchers, B. & Thurber, C.H., 2018. *Parameter Estimation and Inverse Problems*, pp. 93, Elsevier.
- Balkov, E. *et al.*, 2019. High-precision magnetic survey with UAV for the archaeological barrows at Novaya Kurya monument in western Siberia, in *First EAGE Workshop on Unmanned Aerial Vehicles*, Vol. 2019, pp. 1–5, European Association of Geoscientists & Engineers.
- Bhattacharyya, B. & Chan, K., 1977. Reduction of magnetic and gravity data on an arbitrary surface acquired in a region of high topographic relief, *Geophysics*, **42**(7), 1411–1430.
- Cowan, D., Baigent, M. & Cowan, S., 1995. Aeromagnetic gradiometers? a perspective, *Explor. Geophys.*, **26**(3), 241–246.
- Døssing, A., Silva, E.L.S.D., Martelet, G., Rasmussen, T.M., Gloaguen, E., Petersen, J.T. & Linde, J., 2021. A high-speed, light-weight scalar magnetometer bird for km scale UAV magnetic surveying: On sensor choice, bird design, and quality of output data, *Remote Sens.*, **13**(4), 649.
- Fedi, M., Rapolla, A. & Russo, G., 1999. Upward continuation of scattered potential field data, *Geophysics*, **64**(2), 443–451.
- Hansen, R. & Miyazaki, Y., 1984. Continuation of potential fields between arbitrary surfaces, *Geophysics*, **49**(6), 787–795.
- Heincke, B. *et al.*, 2019. Developing multi-sensor drones for geological mapping and mineral exploration: setup and first results from the MULSEDRO project, *GEUS Bull.*, **43**, 1–5.
- Hood, P., 1965. Gradient measurements in aeromagnetic surveying, *Geophysics*, **30**(5), 891–902.
- Hood, P., 1981. Aeromagnetic gradiometry: a superior geological mapping tool for mineral exploration programs, in *SQUID Applications to Geophysics*, eds Weinstock, H. & Overton, W.C., Jr., Society of Exploration Geophysicists.
- Hood, P. & Teskey, D., 1986. Helicopter-borne aeromagnetic gradiometer surveys: A progress report, in *SEG Technical Program Expanded Abstracts 1986*, pp. 152–155, Society of Exploration Geophysicists.
- Hood, P. & Teskey, D., 1989. Aeromagnetic gradiometer program of the Geological Survey of Canada, *Geophysics*, **54**(8), 1012–1022.
- Hood P. *et al.*, &, 1979. *Aeromagnetic gradiometer survey, White Lake, Ontario*.
- Jackisch, R. *et al.*, 2019. Drone-borne hyperspectral and magnetic data integration: Otanmäki Fe-Ti-V deposit in Finland, *Remote Sens.*, **11**(18), 2084.
- Kolster, M.E. & Døssing, A., 2021a. Scalar magnetic difference inversion applied to UAV-based uxo detection, *Geophys. J. Int.*, **224**(1), 468–486.
- Kolster, M.E. & Døssing, A., 2021b. Simultaneous line shift and source parameter inversion applied to a scalar magnetic survey for small unexploded ordnance, *Near Surf. Geophys.*, **19**(6), 629–641.
- Kolster, M.E., Wigh, M.D., Lima Simões da Silva, E., Bjerg Vilhelmsen, T. & Døssing, A., 2022. High-speed magnetic surveying for unexploded ordnance using UAV systems, *Remote Sens.*, **14**(5), 1134.
- Le Maire, P., Bertrand, L., Munsch, M., Diraison, M. & Géraud, Y., 2020. Aerial magnetic mapping with an unmanned aerial vehicle and a fluxgate magnetometer: a new method for rapid mapping and upscaling from the field to regional scale, *Geophys. Prospect.*, **68**(7), 2307–2319.
- Malehmir, A., Dynesius, L., Paulusson, K., Paulusson, A., Johansson, H., Bastani, M., Wedmark, M. & Marsden, P., 2017. The potential of rotary-wing UAV-based magnetic surveys for mineral exploration: a case study from central Sweden, *Leading Edge*, **36**(7), 552–557.
- Martelet, G., Gloaguen, E., Døssing, A., Silva, E. L. S.d., Linde, J. & Rasmussen, T.M., 2021. Airborne/UAV multisensor surveys enhance the geological mapping and 3d model of a pseudo-skarn deposit in Ploumanac’h, French Brittany, *Minerals*, **11**(11), 1259.
- Ray, R.D., 1984. Continuation by integral equation methods: a note on surface integration over the double layer, *Pure appl. Geophys.*, **122**(5), 725–730.
- Salmon, G., 1912. *A Treatise on the Analytic Geometry of Three Dimensions*. Hodges, Smith, & Co., Dublin.
- Scrivens, S., Geo, P., House, R.R.C.M., Map, S.L.R. & Properties, H.L.G., 2015. Technical survey report, gradient magnetic geophysical survey, Ioraine property, *Eagle Geophysics Technical Report*, pp. 40, Eagle Geophysics.
- Teskey, D., Hood, P., Morley, L., Gibb, R., Sawatzky, P., Bower, M. & Ready, E., 1993. The aeromagnetic survey program of the Geological Survey of Canada: contribution to regional geological mapping and mineral exploration, *Can. J. Earth Sci.*, **30**(2), 243–260.
- Walter, C., Braun, A. & Fotopoulos, G., 2019a. Spectral analysis of magnetometer swing in high-resolution UAV-borne aeromagnetic surveys, in *2019 IEEE Systems and Technologies for Remote Sensing Applications Through Unmanned Aerial Systems (STRATUS)*, pp. 1–4, IEEE.
- Walter, C., Braun, A. & Fotopoulos, G., 2020. High-resolution unmanned aerial vehicle aeromagnetic surveys for mineral exploration targets, *Geophys. Prospect.*, **68**, 334–349.
- Walter, C.A., Braun, A. & Fotopoulos, G., 2019b. Impact of three-dimensional attitude variations of an unmanned aerial vehicle magnetometry system on magnetic data quality, *Geophys. Prospect.*, **67**(2), 465–479.